Synthesis and characterization of inverse hybrid perovskites

Ewout van der Veer
e.van.der.veer.1@student.rug.nl

December 5, 2019

Abstract

This report describes attempts to synthesize hybrid as well as inorganic antiperovskite materials. These attempts were unsuccessful in the production of real antiperovskites, but the synthesis of several other compounds is reported. Firstly, the iodide salt of trimethylammonium-N-oxide was synthesized and structurally and thermally characterized using single-crystal x-ray diffraction and differential thermal analysis. This salt was found to assume a monoclinic structure consisting of layers of iodide ions and bilayers of hydrogen bonded trimethylamine-N-oxide molecules along the **c** direction. The exact mechanism of thermal decomposition of the salt remains unclear.

Melt crystallization of sodium iodide and sodium sulfide—reagent for the synthesis of the antiperovskite sodium sulfoiodide—led to the formation of sodium sulfate.

Finally, flux growth of the antiperovskite sodium oxyiodide yielded a small quantity of sodium orthoperiodate. The structure of this compound, which was not previously described in the literature, was solved from single-crystal x-ray diffraction data. The compound was found to be isostructural with previously reported alkali metal perrhenates.

This report can serve as a starting point for further investigation into inorganic and inverse hybrid perovskites.

Contents

List of Figures

List of Tables

1 Introduction

Solar energy is an increasingly popular method of generating electricity. Most commercially available solar cells today use silicon technology, but newer technologies have been attracting much research attention in recent years, offering lower cost and easier processing.[1] Among these are hybrid organic-inorganic materials which incorporate both organic and inorganic ions into their structure. These materials have been known for a relatively long time, but have only recently been used for photovoltaic applications. Although these materials offer high efficiency and processability, they suffer from stability problems in the presence of light or moisture.[1,2] A new class of materials, *inverse hybrid perovskites*, has been theoretically predicted to offer greater stability in these conditions. The work described in this report had the goal of synthesizing such an inverse hybrid perovskite.

The remainder of this chapter will explain some of the theoretical background of hybrid solar cells and inverse hybrid perovskites, chapter 2 contains a description of the experimental work done during this project, chapter 3 reports and discusses the results that were obtained and chapter 4 contains a conclusion and recommendations for further investigation.

1.1 Hybrid perovskites

The term *perovskite* originates from the (inorganic) mineral calcium titanate ($CaTiO_3$), but is now used to describe a class of compounds consisting of hundreds of different materials. All of these have a structure similar to that of calcium titanate, though their properties can vary widely: perovskites have been found and synthesized which exhibit insulating, semiconducting, conducting, superconducting, piezoelectric, thermoelectric and antiferromagnetic behavior.[1]

In general, the composition of perovskite materials is denoted ABX_3, where A and B are (often transition metal or alkali metal) cations and X is an anion (usually O^{2-} or a halide anion). The unit cell of this structure consists of a BX_6 octahedron with the A cation on the vertices of the unit cell, in the cavities between the octahedra. The structure may be cubic, but many perovskite materials show distorted structures as a result of cation displacements or octahedral tilting.[3,4] An example of a cubic perovskite structure and a distorted perovskite are shown in figure 1.

The inorganic ions in traditional perovskites may be replaced by organic ions, yielding *hybrid organic-inorganic perovskites* (HOIPs).[4] Usually, ions on the A site or the X site are replaced. The A site cation is commonly replaced by an alkylammonium ion and the X site by negatively charged organic linkers such as the azide, cyanide and borohydride anions.[4] The structural variation in HOIPs is often more complex than in inorganic perovskites due to the chemical properties of the organic cation itself, its ability to engage in bonding, more complicated octahedral tilting, etc.[4] As a result, HOIPs can exhibit properties not found in inorganic perovskites, such as ferroic and multiferroic behavior.[4] In particular, hybrid halide perovskites have been found in recent years to have the potential to show very high photovoltaic performance, which I will discuss in section 1.1.2.

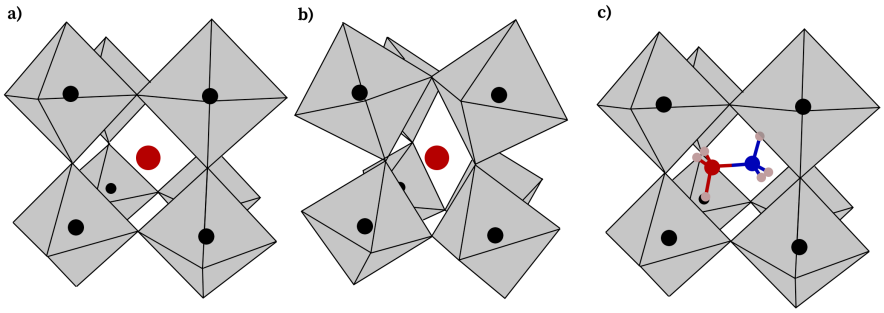

Figure 1: Crystal structures of three types of perovskite structures: (a) the cubic unit cell of an undistorted perovskite, (b) the pseudo-cubic unit cell of a perovskite with octahedral tilting and (c) a hybrid organic-inorganic perovskite. In each case, the B site ion is shown as a black dot, the BX_6 octahedra in grey and the A site ion using blue and red.

1.1.1 Silicon solar cells

Traditional photovoltaic cells often use silicon as the photosensitive material. These cells consist of a layer of silicon covered on both sides with electrodes and on the front with an antireflective coating.[5] The layer of silicon has been doped on one side with a p-type dopant and on the other with an n-type dopant, creating a p-n junction. An energy band diagram of the p-n junction and a schematic depiction of the processes involved in energy generation in the solar cell is shown in figure 2.

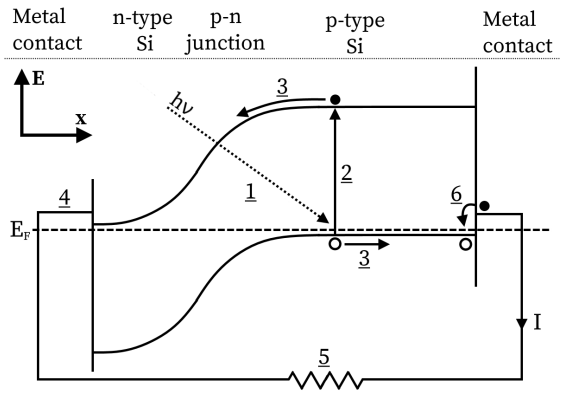

Figure 2: Band structure of a p-n junction inside a silicon solar cell. Absorption of light occurs through six steps: 1. A photon is absorbed in the p-type side of the junction, 2. an electron is excited into the conduction band, 3. the electron and hole move to the n-type and p-type sides of the junction due to the built-in field, 4. the electron flows into the electrical contact, 5. a load is powered by decreasing the energy of the electron and 6. the electron and hole recombine at the electrical contact on the p-type side.

When a photon of light hits the solar cell, it can be transmitted into the cell and be absorbed near the p-n junction by exciting an electron from the valence band into the conduction band.

As a result, a free electron and a free hole are formed. Assuming the photon is absorbed on the p-type side of the junction, the electron—which is the minority carrier in p-type silicon—will be accelerated towards the n-type side by the built-in electric field of the p-n junction, whereas the hole—the majority carrier—remains on the p-type side. The electron can subsequently travel to the electrical contact on the n-type side, then through some electrical load which consumes the electron's energy. Finally, the electron recombines with the hole at the electrical contact on the p-type side of the solar cell, completing the circuit.[6]

Due to a combination of factors, all sunlight that falls on a solar cell cannot be converted to electricity. These factors are:[7]

- Only some photons in sunlight have a sufficient energy to excite an electron across the band gap of silicon. These photons cannot be absorbed and used to generate electricity.
- When a photon is absorbed which has an energy larger than the band gap, an electron is excited to a state above the lowest empty state in the conduction band. After excitation, the electron relaxes nonradiatively to this state. Hence, the electron loses energy which cannot be used to power an electrical load.
- Recombination of the electron and hole generated by excitation releases energy which is emitted from the cell in the form of another photon. This energy is lost and cannot be used to generate electricity.

Considering these factors together, one can show that the maximum efficiency of a single-junction semiconductor solar cell in normal sunlight is 33.7 % assuming the band gap of the material is 1.34 eV.[7] This fundamental limitation to the efficiency of a solar cell is known as the *Shockley-Queisser limit*.

1.1.2 Hybrid perovskite solar cells

Hybrid perovskite materials have been researched in recent years as alternative solar cell materials to replace silicon. This line of investigation grew from research done on so-called *dye-sensitized solar cells* (DSSCs).[1] Such cells are constructed from mesoporous n-type titania covered in a thin layer of a photoabsorbing dye and submerged in an electrolyte. Transparent electrodes make contact to the titania and electrolyte layers.[8] The dye absorbs photons from sunlight, which excites electrons from its highest occupied molecular orbital (HOMO) into its lowest unoccupied molecular orbital (LUMO). These electrons are subsequently injected into the conduction band of titania, which lies at a slightly lower energy than the LUMO of the dye.[8] These electrons are then transported to the electrode and through an electrical circuit, where they power a load. The electrons arrive back to the cell at the other electrode, where they reduce triiodide (I_3^-) ions present in the electrolyte to iodide (I^-) ions. These ions diffuse through the electrolyte towards the dye, where they are oxidized back to triiodide ions, delivering the electrons back to the dye in its HOMO.

The principal drawback of these DSSCs is that the photosensitive dye is not sufficiently absorbing, requiring the use of impractically thick dye layers.[1] An alternative was found in the form of the hybrid perovskites $CH_3NH_3PbX_3$ where X=I, Br.[1] In these *perovskite-sensitized solar*

cells (PSSC), the perovskite layer fulfills the role of the dye in DSSCs and is coupled with the same titania electron transporting layer and an electrolyte. This electrolyte can contain the same iodide/triiodide couple as in DSSCs, but cells made in this way were found to degrade over time due to dissolution of the perovskite into the electrolyte.[1] Alternative solid-state electrolytes, such as 2,2',7,7'-tetrakis[N,N-di(4-methoxyphenyl)amino]-9,9'-spirobifluorene or *spiro-OMeTAD*,[1] were developed to solve this problem.[1,2] A schematic depiction of a DSSC or PSSC is shown in figure 3(a).

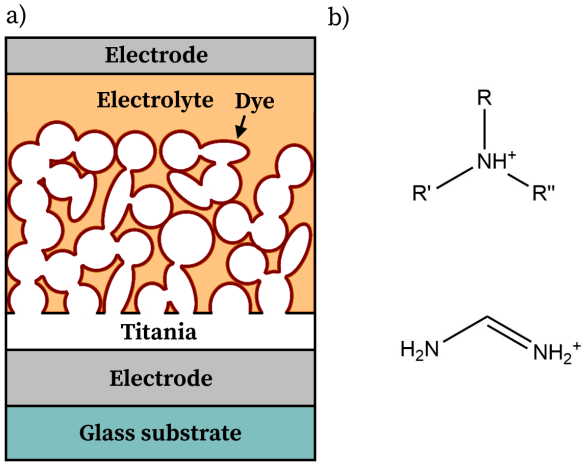

Figure 3: (a) Drawing of the structure of a dye-sensitized solar cell. A perovskite-sensitized solar cell has the same structure, but has its dye replaced by a perovskite absorbing layer. The electrolyte may be liquid or solid. Adapted from Snaith (2013)[1]. (b) Chemical structures of the alkylammonium and formamidinium ions. In the case of methylammonium, R = CH_3 and R' = R" = H.

Another class of perovskite-based solar cells uses alumina as a substrate for the perovskite layer instead of titania.[1,2] The conduction band of alumina is too high in energy for it to act as an electron transporting layer. Nevertheless, solar cells constructed in this way, called *meso-superstructured solar cells* (MSSCs), have been found to exhibit good photovoltaic performance.[1] In these cells, electron transport occurs through the perovskite layer itself, which gives these cells a relatively high open-circuit voltage and hence potentially a high efficiency.[1]

The range of perovskite materials used for the production of solar cells has been relatively limited, employing primarily the following ions:[4]

A-site methylammonium, formamidinium (see figure 3(b))

B-site Pb^{2+}, Sn^{2+}

X-site Cl^-, Br^-, I^-

The A-site is limited to the smallest organic cations due to the size of the cavity between the BX_6 octahedra. Larger cations lead to layered structures which show diminished transport properties.[4]

Perovskite materials are useful for solar cells due to their strong optical aborption, which allows for the fabrication of thinner layers and the collection of more photogenerated carriers.[2]

Furthermore, the achievable efficiency of a perovskite solar cell is predicted to be high due to its high open-circuit voltage.[1] In fact, perovskite solar cells have already attained a higher efficiency than single-junction silicon cells.[9] Additionally, perovskite solar cells can be processed easily at a low cost and the required starting materials are available in abundance.[1,4]

Nonetheless, two main limitations to perovskite solar cells can be identified: their toxic lead or tin B-site cations and their instability under atmospheric conditions.[4] These problems can be addressed by encapsulation of the cell, but chemical modification of the perovskite layer is also being investigated as a means to improve device stability.[4] Options include mixed cation perovskites, 2D layered perovskites, perovskites using germanium instead of lead or tin and double perovskites where lead or tin is replaced by a mixture of monovalent and trivalent cations.[4] A recently proposed method of improving the stability of hybrid perovskite solar cells is the use of inverse hybrid perovskites, in which the positions of the cation and anions are swapped. These materials are the topic of section 1.3.

1.2 Goldschmidt tolerance factor

It is not obvious that the perovskite structure described above is always preferred over other possible structural arrangements of a given combination of ions. The *Goldschmidt tolerance factor* (t) has long been used to make this determination. It was first devised based on geometrical considerations of the ions, which are treated as hard spheres. The tolerance factor is calculated with equation 1[10,11] and uses the ionic radii of the constituent ions (r_A, r_B and r_X, generally obtained from Shannon (1976)[12]).

$$t = \frac{r_A + r_X}{\sqrt{2}(r_B + r_X)} \tag{1}$$

For inorganic materials, cubic perovskite structures are generally found for $0.9 < t < 1$. Larger values of t lead to hexagonal perovskite structures with layers of face-sharing octahedra. Conversely, when $0.8 < t < 0.9$, the material is found in a distorted perovskite structure. Even smaller values of the tolerance factor yield completely different non-perovskite structures due to the similar sizes of the A and B site ions.[10,11] In addition to the tolerance factor, Li et al. (2008)[13] defined an additional parameter, the octahedral factor (μ), which is the ratio of the ionic radii of the B-site and X-site ions. They were able to use a combination of the tolerance factor and the octahedral factor to accurately determine the structure of a large number of materials.

The concept of a tolerance factor was extended to organic-inorganic hybrid materials by Kieslich et al. (2014)[10]. The calculation of tolerance factors for these materials is complicated by the fact that the ionic radius of organic ions is difficult to define due to bonding interactions with the counterion and anisotropy of the molecule. Nonetheless, by assuming full rotational freedom of the molecular ion in the structure—an assumption supported by literature[14])—they were able to determine ionic radii for eleven common nitrogen-based cations with values ranging from 146 pm for the ammonium ion to 292 pm for tetramethylammonium. A list of effective ionic radii of organic cations is provided in table 1.

Cation	Formula	Effective radius (pm)
Ammonium	$[NH_4]^+$	146
Hydroxylammonium	$[H_3NOH]^+$	216
Methylammonium	$[(CH_3)NH_3]^+$	217
Hydrazinium	$[H_3N–NH_2]^+$	217
Azetidinium	$[(CH_2)_3NH_2]^+$	250
Formamidinium	$[NH_2(CH)NH_2]^+$	253
Imidazolium	$[C_3N_2H_5]^+$	258
Dimethylammonium	$[(CH_3)_2NH_2]^+$	272
Ethylammonium	$[(C_2H_5)NH_3]^+$	274
Guanidinium	$[C(NH_2)_3]^+$	278
Tetramethylammonium	$[(CH_3)_4N]^+$	292

Table 1: Effective ionic radii of organic cations. Reproduced from Kieslich et al. (2014)[10].

The general trends observed for inorganic materials are still valid for organic-inorganic hybrids. Perovskite structures are expected for $0.8 < t < 1$ with non-perovskite structures found for smaller tolerance factors.[10,11] Values of the tolerance factor larger than unity lead to the formation of hexagonal and low-dimensional phases, such as Ruddlesden-Popper-type phases.[11,14]

1.3 Theoretical predictions of inverse hybrid perovskites

A combination of the antiperovskite structure with an organic ion, as in hybrid perovskites, was reported in a series of publications by Gebhardt and Rappe.[15–17] They study these X_3BA-type materials, which they term *inverse hybrid perovskites*, using density functional theory. A wide range of compositions with different A-site and B-site anions was investigated, keeping a fixed X site organic cation: the small methylammonium ion. However, the tolerance factor of these structures is relatively insensitive to the size of the organic cation as it appears in both the numerator and the denominator of the formula.

The X_3BA materials were found to adopt either a perovskite structure or a number of other related structures (most notably a $CaIrO_3$-type structure, which is analogous to the Ruddlesden-Popper phase in other perovskites[15]) depending on the value of the tolerance factor. For $t > 0.76$, perovskite structures are formed; for smaller values, other structures are generally preferred.

Considering the choice of A-site and B-site anions, Gebhardt and Rappe[16] note that the A-site is larger and will more easily accommodate a larger divalent anion. However, the Coulombic attraction between the A-site and the organic cation is weaker, favoring the monovalent anion. Hence, these effects are in competition, contrary to ordinary perovskites, and the occupation of each of these sites is not obvious. Smaller B-site anions will always stabilize the perovskite structure due to an increase of the tolerance factor.[15,16]

A wide range of different properties could be obtained depending on the choice of anions.[15,17] Those compositions which used chalcogenides and halides as the divalent and monovalent anions generally had large band gaps of 2.5 eV or more. When heavier elements were used, a small band gap was present due to the splitting of bands as a result of spin-orbit coupling. Yet

other compositions, such as those of group 13 elements and halides, showed metallic behavior. Additionally, many of these compositions had polar structures due to a displacement of the B-site anion, potentially allowing for their use as ferroelectric materials. Apart from p-block elements, transition metals were also studied as A-site and B-site anions.[17] Inverse hybrid perovskites using transition metals appear to be attractive for photovoltaic applications due to their intermediate band gaps, which result from crystal field splitting of their partially filled d-shell. Unfortunately, these results remain somewhat academic as only gold and platinum have been stabilized as monatomic anions in the solid state (in both cases requiring harsh reaction conditions).[18] It should be noted, however, that transition metals have been routinely found in negative oxidation states as part of ligand-stabilized coordination complexes.[18] Hence, such complexes might be useful as polyatomic negative ions in inverse hybrid perovskites (in fact, this is the approach taken in the few experimental reports of IHPs which have been published to date).

An important advantage of inverse hybrid perovskites is their predicted improved stability towards moisture and light, which can lead to degradation in normal hybrid perovskites.[19] This improvement was attributed to the bonding pattern of the organic cation on the X-site, which is not present when the organic group is on the A-site.[16]

These theoretical findings have not been experimentally confirmed due to the limited availability of reports on the synthesis of such compounds. Those IHPs that have been produced[20–22] use polyatomic anions whose ionic radius is especially difficult to determine[16] so tolerance factors for these compounds have not been calculated.

The first report of an inverse hybrid perovskite[22] used the tetrathiavalenium cation radicals and hexanuclear molybdenum halide anions which crystallized in a rhombohedrally distorted inverse perovskite phase grown electrochemically. The unpaired spins led to antiferromagnetic ordering at low temperatures. In 2018, two publications[20,21] reported on inverse hybrid perovskites using trimethylamine as the cation and manganese halides as the anions. These materials crystallized in a hexagonal phase, with a structure consisting of chains of trimethylammonium cations and manganese trihalide anions separated by isolated manganese tetrahalide anions. Although these materials were reported to be antiperovskites, their structure deviates strongly from that of ordinary antiperovskites. Nonetheless, these materials showed moderate ferroelectric behavior well above room temperature and optical absorption and photoluminescence in the visible region, making them interesting for photovoltaic applications.

1.4 Crystal growth techniques

Not many reports on the crystal growth of inverse hybrid perovskites are available in the literature, but the crystal growth techniques used for ordinary hybrid perovskites may also be applicable to IHPs. Below, I will briefly discuss several common growth techniques that are used for hybrid perovskite crystals. In general, crystal growth can be performed in the vapor, liquid or solid phase. Hybrid perovskite single crystals have only been grown using solution-based techniques,[23] so I will limit the discussion to those.

Hybrid organic-inorganic perovskite crystals have been grown using four main techniques.

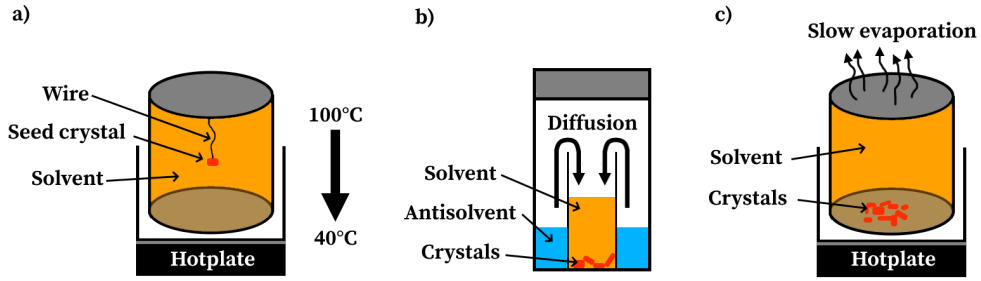

Figure 4: Three common crystallization methods for hybrid perovskites: (a) bottom seeded solution growth, (b) antisolvent vapor-assisted crystallization and (c) slow evaporation.

These are:[23,24]

- Cooling of HX solutions
- Inverse temperature crystallization
- Antisolvent methods
- Slow evaporation

Each of these methods relies on slowly decreasing the solubility of the product in the growth medium, which causes crystals of that product to grow.

The most common growth technique for methylammonium lead halide hybrid perovskite crystals involves cooling a saturated, aqueous solution of HX, where X is a halide. Pb^{2+} and $CH_3NH_3^+$ are dissolved in this solution, which is then cooled from approximately 100 °C to 40 °C in the presence of a seed crystal. Methylammonium lead halides are less soluble at lower temperatures, so a crystal grows on the seed.[23,24] The seed crystal may be introduced into the solution in two ways. In bottom-seeded solution growth (BSSG, see figure 4(a)), the seed crystal is placed in the solution on top of a tray or suspended on a wire and the solution is cooled in its entirety. In top-seeded solution growth (TSSG), small crystals of the product are placed at the bottom of the solution and a seed is placed at the top. The solution is heated at the bottom to dissolve the crystals. At the top, it is cooled so the product crystallizes onto the seed. Both of these methods have been used to grow single crystals up to centimeter sizes.[23,24] Solution growth is a simple and convenient method for growing hybrid perovskite single crystals with a high quality and large size. However, the method is rather slow (months) and requires finding an appropriate solvent.[24]

Inverse temperature crystallization (ITC) is, in some sense, the inverse of normal solution growth. It exploits the fact that hybrid perovskites have an abnormal solubility in some solvents, such as N,N-dimethylformamide (DMF), dimethyl sulfoxide (DMSO) or γ-butyrolactone (GBL). In these solvents, the solubility of the perovskite decreases with increasing temperature.[23,24] Hence, crystals can be grown by introducing a seed into a low-temperature (60 °C) saturated solvent and then increasing the temperature to approximately 100 °C.[23] Millimeter-sized crystals could be grown using this method in three hours.[23] A drawback is that solvent adduct phases are known to form in some systems, which require post-annealing to obtain the desired perovskite product.[24]

In the case of anti-solvent methods, the supersaturation required to grow crystals is not achieved through changing the temperature, as was the case in the two methods described above, but through the addition of a second solvent which does not dissolve the product.[23,24] This method is depicted in figure 4(b). The slow addition of such an anti-solvent will reduce the solubility, which ultimately leads to supersaturation of the solution, allowing for growth of the crystal on a seed. Common solvents used for the growth of hybrid perovskite crystals are DMF, DMSO and GBL, which are combined with anti-solvents such as chlorobenzene, benzene and diethyl ether.[23] An alternative to the ordinary anti-solvent method is *antisolvent vapor-assisted crystallization* (AVC), which relies on the evaporation of the anti-solvent and its subsequent diffusion into a volume of the solvent which has the product dissolved in it.[23–25] This method allows for a slow and steady rate of addition of anti-solvent to the solution, leading to high quality, millimeter-size single crystals.[25] Yet another variant on the anti-solvent method involves two layers of different solvents placed on top of each other in a reaction vessel.[26] The inorganic precursor is dissolved in an aqueous solution on the bottom, whereas the organic precursor is added to a methanol layer on top. Crystals of the hybrid perovskite form at the interface between the layers.[26]

The final solution growth method for hybrid perovskite crystals is conceptually the simplest. A saturated solution of the product is made and then left to evaporate. As some of the solvent is removed, the solution becomes supersaturated and crystals can grow (figure 4(c)). This method has the advantage of being very efficient and usable for a large number of compounds, but it is difficult to accurately control.[24] Slow evaporation was the method used for the synthesis of the inverse hybrid perovskite reported by Wei et al. (2018)[20] (see section 1), which shows that this method is applicable to compounds other that ordinary hybrid perovskites.

1.5 Aim of the project

The initial aim of this project was to synthesize an inverse hybrid perovskite, to determine its structure using x-ray diffraction analysis and to measure its optical properties. The focus was on the synthesis of trimethylammonium oxyiodide and methylammonium oxyiodide as these were theoretically predicted to be thermodynamically stable and crystallize in the inverse hybrid perovskite structure.

After efforts to synthesize this compound proved unsuccessful, the focus shifted to the synthesis of inorganic alkali metal oxyhalide antiperovskites, which had been reported to absorb visible light, but were otherwise not extensively studied.

2 Experimental

The experimental work for this project is divided into two parts. The first aimed to directly synthesize an inverse hybrid perovskite, namely (tri)methylammonium oxyiodide. The second involved the synthesis of the inorganic antiperovskites sodium sulfoiodide and sodium oxyiodide; these syntheses were inspired by earlier reports of the synthesis of similar compounds.[27–29] The two parts will be discussed in turn.

2.1 Synthesis of intermediate products

Several intermediate products were synthesized for use in subsequent product syntheses. These are:

- Trimethylamine-N-oxide
- Trimethylammonium oxide
- Methylammonium nitrate

The procedure for the fabrication of trimethylamine-N-oxide (TMANO) was based on a report by Pearson and Yamamoto (2010)[30]. 35 mL of hydrogen peroxide (0.343 mol, H_2O_2, 30% in water, 20 mol.% excess, Merck) was added to an erlenmeyer flask on ice. 67 mL of trimethylamine solution (0.281 mol, $(CH_3)_3N$, 4.2M in ethanol, Aldrich) was added slowly while stirring vigorously. The solution was then stirred for three days at room temperature. The product was obtained by distillation of the solvent. Two fractions were obtained: one at 79 °C which consisted of ethanol. The other came over at 98-100 °C and was strongly basic. This fraction contained water and remaining trimethylamine. The distillation was stopped when no more distillate came over. Yellow liquid still remained in the distillation flask. Upon cooling, a precipitate formed. The precipitate was recrystallized from ethanol/diethyl ether. After filtration and thorough washing with diethyl ether, the product was obtained as off-white needle-like crystals. 20.064 g (representing a yield of approximately 65%) of trimethylamine-N-oxide dihydrate was obtained. The product is dried *in vacuo* and subsequently characterized using powder x-ray diffraction (PXRD) and differential scanning calorimetry/thermogravimetric analysis (DSC-TGA).

An attempt was made to synthesize trimethylammonium oxide by dissolving 1 g of silver oxide (4.32 mmol, Ag_2O) and 0.3 g trimethylamine hydrochloride (3.14 mmol, $(CH_3)_3N \cdot HCl$, 98%, Aldrich) in approximately 25 mL of water. The trimethylamine hydrochloride dissolved completely, but the silver oxide remained largely undissolved. The suspension was heated to 80 degrees and stirred for several hours. The solution was filtered and the filtrate was evaporated. Little to no product was obtained. It is likely that trimethylammonium oxide is too unstable to be synthesized due to the basicity of the oxide anion. Hence, no further attempts were made to synthesize this compound.

The synthesis of methylammonium nitrate (MAN) was based on a report by Kurniadi and Brower (1994)[31]. 52 mL of methylamine (0.418 mol, CH_3NH_2, 33 wt.% in ethanol, Aldrich) was added to a glass beaker in an ice bath. Nitric acid (>65% in water, Boom BV) was added to the solution slowly to neutralize it. The solution was heated on the hotplate to remove the solvent. After 2h it appeared that no solvent had been removed, so the solution was cooled to room

temperature, causing it to crystallize into an orange, firm, gel-like structure. An attempt was made to recrystallize the product from tert-butanol, but this was not successful. The product was then left to dry *in vacuo* overnight. Another recrystallization was attempted from ethanol, but the compound did not dissolve sufficiently. No further purification was attempted. The synthesized material had a melting point between 55 and 65 °C and had the appearance of a wet, yellow sludge. 28.27 g of MAN was obtained, representing a yield of 74%. The as synthesized material was characterized by DSC-TGA at 5 °C/min and PXRD.

2.2 Synthesis of trimethylammonium-N-oxide iodide

4.919 g of previously synthesized trimethylamine-N-oxide dihydrate (37.7 mmol, $(CH_3)_3NO{\cdot}2H_2O$) was dissolved in 2.882 mL of HI solution (21.8 mmol, HI, 57 wt.% in water, Arcos Organics) in a test tube while stirring. The solution was heated to 70 °C and stirred for 1 h. The solution was decanted into a glass beaker, cooled to 60 °C and left overnight to evaporate the solvent. The brown solid left after evaporation of the solvent was washed very thoroughly with diethyl ether and dried in vacuum. A yellow-brown, foul smelling solid product was obtained. The product was subsequently washed with N,N-dimethylformamide (DMF) and diethyl ether. A large amount of the product was lost due to dissolution in DMF. However, washing yielded a white solid product without any odor. Single crystals of the product were grown by dissolving the cleaned powder in DMF at 60 °C, then lowering the temperature at approximately 5 °C/h to room temperature. The resulting crystals were filtered, washed with diethyl ether and stored in the refrigerator. They were transparent and plate-like and broke easily.

A few of the crystals were crushed into a powder in an agate mortar for powder x-ray diffraction. A diffractogram was collected between 5° and 80° 2θ ($\Delta 2\theta = 0.009°$, time/step = 7 s, total time/step = 1330 s, primary Soller slit: 2.5°, divergence slit: 2 mm, antiscatter slit: 1 mm).

DSC-TGA of a few other crystals was performed between 30 °C and 300 °C with a heating rate of 5 °C/min under and argon flow of 100 mL/min. The total mass of these crystals before measurement was 5.005 mg.

Finally, a crystal was selected for single-crystal x-ray diffraction. The size of this crystal was 0.22×0.32×0.50 mm.

2.3 Methylammonium oxyiodide

The previously synthesized methylammonium nitrate was used to attempt a synthesis of methylammonium oxyiodide, based on a report of the synthesis of bismuth oxyiodide.[32] 5 g (53 mmol) of methylammonium nitrate was dissolved in 100 mL of 3 mol/L nitric acid. A 2 mol/L solution of sodium hydroxide was added to adjust the pH to 3. The solution was stirred for 1 h. The report by Li et al. (2011)[32] indicates that a precipitate should form, but no such precipitate was observed here. Hence, the synthesis was abandoned.

A second attempt at the synthesis of methylammonium oxyiodide was based on the earlier synthesis of trimethylammonium-N-oxide iodide. 5 g (53 mmol) of previously synthesized methy-

lammonium nitrate was dissolved in 2.338 mL of 57 wt% aqueous hydroiodic acid at 90 °C. The solution was stirred at 90 °C for 40 min, then cooled slowly to room temperature overnight. A precipitate formed and the solution had a dark brown color. The precipitate was redissolved by adding a small amount of water. The solution was then drop cast onto glass microscope slides at 100, 120 and 140 °C and dried for 30 min at the same temperature. Deliquescent solids were obtained. The solids formed at 140 °C were used for DSC-TGA and PXRD.

2.4 Synthesis of sodium sulfoiodide

For the synthesis of sodium sulfoiodide, sodium sulfide (Riedel-de Haën, Na_2S, 60-62 %) and sodium iodide (Merck, NaI, 99.5 %) were dried at 200 °C in vacuum for approximately 16 h. The oven was cooled down and backfilled with argon. Dry sodium iodide was obtained as a white powder. 2.00 g (13.3 mmol) of the NaI and 1.71 g (13.3 mmol) of Na_2S (assuming a concentration of Na_2S of 61 %) were loaded into an agate mortar and ball milled for 80 min. The mixture, a pale yellow-green powder, was loaded into a platinum crucible and inserted in a tube furnace under argon. The material was heated to 450 °C in 1 h, kept there for 70 h, then cooled to room temperature in 22 h. The crucible with the white powdered product was transported to the glovebox ($c_{H_2O} < 1$ppm, $c_{O_2} < 30$ppm). A part of the product was placed back in the crucible and heated again under argon to 620 °C, melting the material. Crystallization was achieved by cooling to 580 °C in 48 h, then to room temperature in 14 h.

Single-crystal x-ray diffraction was performed on one of the crystals obtained from the melt. The size of this crystal was 0.110×0.210×0.240 mm.

DSC-TGA was done of a crystal between room temperature and 1000 °C at a rate of 20 °C/min under and argon flow of 100 mL/min. The initial mass of the crystal was 5.7161 mg.

Ethanol was added to part of the crystallized product to dissolve any sodium iodide or sodium sulfide that may be present. Most of the product did not dissolve. The product was ground in a mortar and used for energy dispersive spectroscopy to determine its chemical makeup and for powder XRD. The pattern was collected between 5° and 100° 2θ ($\Delta 2\theta = 0.02°$, time/step = 12 s, total time/step = 2280 s, primary Soller slit: 2.5°, divergence slit: 0.2 mm, antiscatter slit: 1 mm).

A second synthesis of sodium sulfoiodide was attempted by mixing sodium sulfide and sodium iodide in a 1:1.05 molar ratio and sealing the mixture in a quartz ampoule. The ampoule was heated to 680 °C in 2 h, kept there for 1 h, then cooled to 550 °C in 70 h. After synthesis, the ampoule was found to have burst during the synthesis. The synthesis was repeated with a smaller amount of material, but the ampoule burst again. No further attempts were made to synthesize sodium sulfoiodide.

2.5 Synthesis of sodium oxyiodide

Sodium oxyiodide was synthesized by solid-state method and flux growth. For the solid-state method, 0.50 g of Na_2O (Alfa Aesar, 80 % Na_2O with 20 % Na_2O_2) was mixed with 1.16 g of NaI (Merck, 7.74 mmol, NaI, 99.5 %) and ground in an agate mortar inside the glovebox ($c_{H_2O} < 1$ppm,

$c_{O_2} < 30$ppm). The mixture was loaded into a platinum crucible inside a glass ampoule. The ampoule was put under vacuum and sealed. The mixture was heated to 450 °C for 50 h and cooled to room temperature in 22 h. The ampoule was removed from the furnace and transported to the glovebox. It was opened and the white, powdered product was removed from the crucible. The solids had formed a white, sintered mass. Some purple discoloration could be seen where the solids touched the platinum crucible.

DSC was done of the white part of the product between 30 and 1000 °C with a rate of 20 °C/min. Powder x-ray diffraction patterns under a Mylar film and EDS spectra were obtained for both the white and purple parts of the product.

For the flux growth, approximately 0.50 g of Na_2O (Alfa Aesar, 80 % with 20 % Na_2O_2) was mixed with an excess (5:1 molar ratio) of NaI (Merck, NaI, 99.5 %) and added to a platinum crucible. The crucible was loaded into a tube furnace and heated to 680 °C under argon in 2 h. It was kept at this temperature for 8 h, then cooled at 5 °C/h to 580 h. It was then cooled to room temperature in 10 h. The crucible was transported to the glovebox ($c_{H_2O} < 1$ppm, $c_{O_2} < 30$ppm) and some of the crystals were removed. The crucible with the remaining crystals was submerged in glycerin to dissolve the sodium iodide flux. A small number of dark brown/black clusters of crystals remained undissolved in the glycerin. These were removed from the glycerin and washed with ethanol. One crystal, with a size of 0.1×0.14×0.1 mm, was selected for single-crystal XRD.

A third synthesis of sodium oxyiodide was attempted by sealing 1 g of sodium oxide (Alfa Aesar, 80 % with 20 % Na_2O_2) and 0.414 g of freshly dried anhydrous sodium iodide (Merck, NaI, 99.5 %) in a quartz ampoule under vacuum. The ampoule was heated in a box furnace to 680 °C in 4 h, kept there for 4 h, then slowly cooled to 550 °C in 70 h. The ampoule was then cooled to room temperature in 10 h. The ampoule was opened in the glovebox ($c_{H_2O} < 0.3$ppm, $c_{O_2} < 0.3$ppm).

2.6 Instrumentation

Powder x-ray diffractograms were collected using a Bruker D8 Advance diffractometer in Bragg-Brentano geometry using a LynxEye position-sensitive detector, CuKα radiation, with a rotating sample and fixed antiscatter and divergence slits.

Differential scanning calorimetry/thermogravimetric analysis was performed using a Texas Instruments SDT 2960 DSC with an argon flow of 100 mL/min in alumina crucibles.

Single-crystal x-ray diffraction measurements were performed using a Bruker D8 Venture diffractometer with a Triumph monochromator and a Photon100 area detector. MoKα radiation was used for the measurement. Crystals were mounted on a 0.5 mm nylon loop using cryo-oil and cooled to 100 K using a Oxford Cryosystems Cryostream Plus.

Qualitative elemental analyses were preformed using energy dispersive spectroscopy (EDS) in an FEI Nova NanoSEM 650 scanning electron microscope equipped with an EDAX EDS detector.

2.7 Software

Single-crystal x-ray diffraction data was collected, integrated and absorption corrected using the Bruker APEXIII software. Structure solution and least squares refinement was performed using the SHELX software package[33] with anisotropic displacement parameters. Methyl-group hydrogens were added in a tetrahedral geometry. During refinement, C-H bond distances were kept fixed while torsion angles were allowed to vary. Other hydrogen atoms were refined independently.

Rietveld refinements of powder x-ray diffractograms were performed using the JANA2006 software.[34]

Drawings of crystal structures were produced using the VESTA software. Plots of data were produced using Origin Pro 8.

3 Results and discussion

3.1 Theoretical reports

The theoretical papers by Gebhardt and Rappe[15–17] contain a large number of different materials which may form inverse hybrid perovskites. The selection of a suitable candidate for synthesis was based on a number of factors. The first was the structure the material was predicted to assume. Many of the materials were calculated to be stable in structures other than ordinary inverse perovskites, such as a $CaIrO_3$-type phase. These materials were initially neglected. Second is the electronic properties of the materials. Two groups can be distinguished among the calculated compounds: semiconducting and metallic. The latter group is not useful for photovoltaic applications so it was not considered further. The third consideration was the chemical feasibility of the material. A number of inverse hybrid perovskites were calculated using transition metals in negative oxidation states which have advantageous band gaps for use in solar cells. However, only a few transition metals (*e.g.* gold) are known to exist as monoatomic anions and only in particular circumstances (*e.g.* as part of CsAu). Hence, it is unlikely that these materials can actually be synthesized. The final decision to attempt the synthesis of methylammonium oxyiodide was made based on which chemicals were available in the laboratory. A small modification was made to this compound by exchanging the methylammonium ion for a trimethylammonium ion as an oxide of this ion can be obtained and it is larger and more spherical which was thought to promote crystallization in the inverse perovskite structure.[35]

3.2 Trimethylammonium-N-oxide iodide

DSC-TGA curves of the trimethylammonium-N-oxide iodide product are shown in figure 5. An initial weight loss and endothermic peak is observed at approximately 130 °C, followed by an exothermic decomposition at 165 °C accompanied by a weight loss of approximately 50 %. Gradual weight loss is observed at higher temperatures without a significant heat flow. Approximately 8.5 % of the initial weight remains after full decomposition. The mechanism of decomposition of the product is unclear. The first weight loss at 130 °C is close to the boiling point of hydroiodic acid as well as the previously reported[36] melting/decomposition point of trimethylammonium-N-oxide iodide. Hence, it may correspond to the melting of the product and loss of some hydroiodic acid. However, not all hydroiodic acid is lost in this transition as a weight loss of only 5 % is observed, despite HI making up approximately 50 % of the mass of the product.

The subsequent decomposition at higher temperatures may follow one of two possible paths found in the literature. The first is simply the further loss of hydroiodic acid from the crystal structure at 165 °C leaving trimethylamine-N-oxide behind, followed by decomposition of this compound up to 300 °C. However, this explanation does not account for the exothermic nature of the loss of HI which is expected to be endothermic. Additionally, trimethylamine-N-oxide decomposed at much lower temperatures (below 220 °C) when it was measured in isolation. Finally, the nature of the remaining 8.5 % of the mass of the product is unexplained.

An alternative reaction mechanism involves the direct decomposition of the hydroiodide

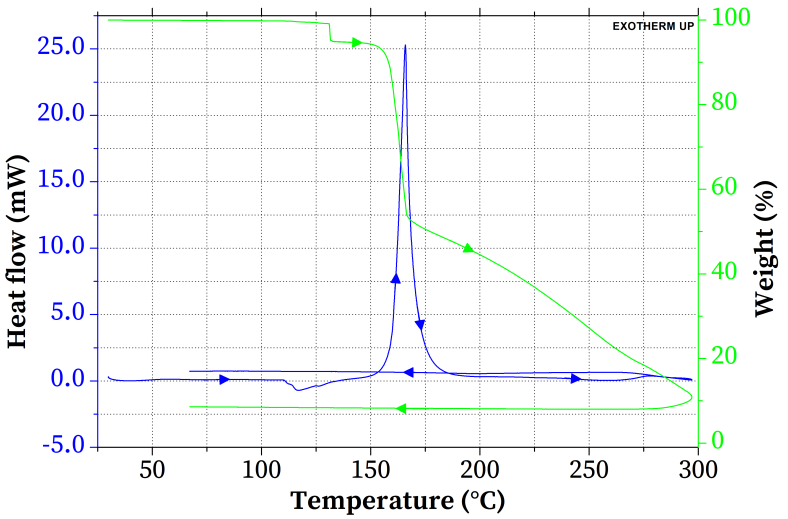

Figure 5: DSC-TGA trace of the trimethylammonium-N-oxide iodide product.

salt.[37] In this case, the trimethylamine-N-oxide molecules react with the iodide ions and protons, forming trimethylamine, elemental iodine and water. Unfortunately, this reaction requires a 1:2 trimethylamine-N-oxide:iodide ion molar ratio be present. This does not concord with the crystal structure and elemental analysis results presented below. Additionally, this reaction does not explain the decomposition at higher temperatures or the remaining mass after decomposition.

In conclusion, neither of these decomposition mechanisms fully accounts for the observed behavior of the product. The true decomposition path may involve a combination of these two or some other reaction altogether. Further research will be required to elucidate this process.

The crystal structure of trimethylammonium-N-oxide iodide as solved by single-crystal XRD at 100 K is shown in figure 6; the cell parameters are listed in table 2. The structure is layered

Table 2: Cell parameters of the structure of trimethylammonium-N-oxide iodide determined from SCXRD at (a) 100 K, (b) 300 K and (c) using Rietveld refinement of the powder pattern.

	100K	**300K**	**Rietveld**
Space group	C2/c	C2/c	C2/c
a	17.8644(18) Å	17.917(2) Å	17.9110(3) Å
b	5.7309(6) Å	5.8171(8) Å	5.818 50(9) Å
c	10.8926(11) Å	11.0506(14) Å	11.056 91(17) Å
a	90°	90°	90°
β	94.688(3)°	94.746(5)°	94.6864(9)°
γ	90°	90°	90°
V	1111.4(2) Å^3	1147.8(3) Å^3	1148.44(3) Å^3

perpendicular to the **c** direction with two layers of trimethylamine-N-oxide molecules bonded together with hydrogen bonds and a layer of iodide anions. The trimethylamine-N-oxide molecules are rotated slightly with respect to each other as a result of the hydrogen bond between them.

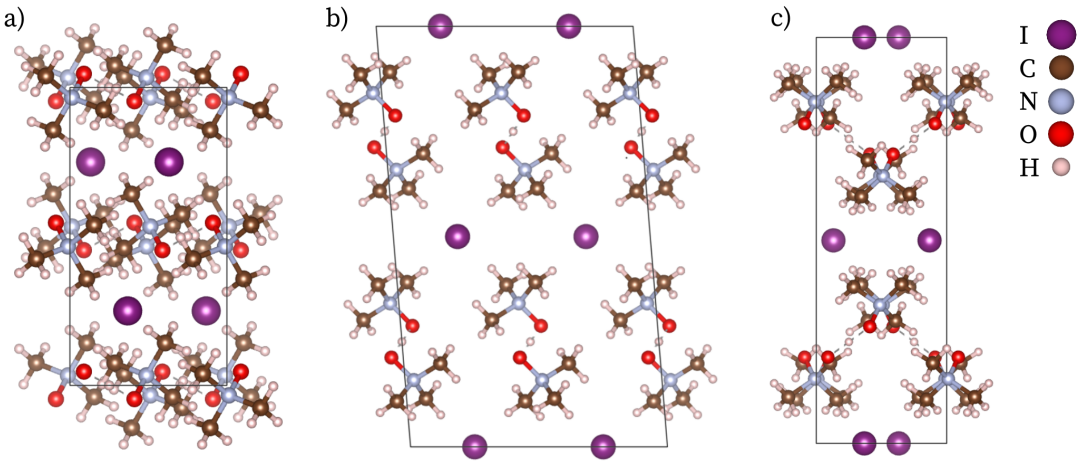

Figure 6: Structure solved from single-crystal XRD data, displayed along the **a**, **b** and **c** directions of the unit cell.

Structure solution at 300 K yielded the same structure with a slightly larger unit cell due to thermal expansion (see table 2). This structure was further refined using powder XRD data collected from a sample of crushed crystals, see figure 7. The geometry of the trimethylamine-N-

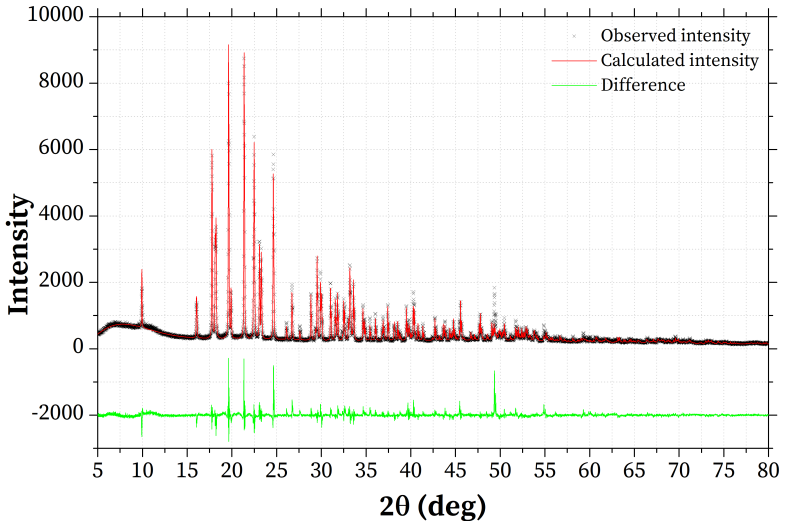

Figure 7: Powder x-ray diffractogram and Rietveld fit of crystallized trimethylammonium-N-oxide iodide

oxide molecule was kept rigid during the refinement, allowing only refinement of the position of the molecule and the iodide ions. The structure refined using Rietveld refinement shows a good fit to the collected pattern and impurity peaks are present above the background level. The final cell parameters obtained from Rietveld refinement are listed in table 2.

The structure solution was further confirmed using elemental (CHN) analysis of the crystals. The results are listed in table 3.

Element	**Measured** [%]	**Expected** [%]
C	25.78	25.90
N	9.93	10.07
H	6.81	6.52

Table 3: Elemental analysis results for trimethylamine-N-oxide. The expected percentages were calculated using the structure solved by SCXRD.

The measured fractions of carbon, nitrogen and hydrogen in the sample are very close to the values expected from the structure presented above. Hence, the structure is likely to be correct.

It is clear that the desired inverse perovskite structure was not formed. This is due to the strong covalent bond between the nitrogen and oxygen atoms. In the inverse perovskite structure, oxygen is present as a more-or-less independent ionic species, which is difficult to achieve from the covalently bonded trimethylamine-N-oxide. Instead, the ionic species trimethylammonium oxide ($(Me_3NH)_2O$) should be used. An attempt was made to synthesize such a salt by a metathesis reaction between silver oxide and trimethylammonium chloride, but this reaction failed. An organic oxide such as trimethylammonium oxide would likely not be stable due to the high basicity of the oxide anion. This leads to the deprotonation of the organic cation, forming hydroxide ions and water. In fact, the formation of a water molecule was also observed in the theoretical calculations of oxide-containing inverse hybrid perovskites (see figure 1(c) of Gebhardt and Rappe (2018)[15]). The basicity of chalcogen anions decreases down the periodic table, so organic sulfides, selenides and tellurides should be more easily attainable. However, the inverse hybrid perovskite structure favors small B-site anions (*i.e.* oxide) as this increases the tolerance factor (see table 1 from Gebhardt and Rappe (2018)[15]).

Fortunately, the inverse hybrid perovskite structure allows for a monovalent anion on the B-site (see section 1.3). Hence, monovalent halide anions—which are much less basic—may provide an alternative to the use of a chalcogen anion on the B-site. In this case, a larger chalcogen dianion can occupy the A-site. An example of such a compound is MA_3FTe, which might be synthetically accessible.

3.3 Methylammonium oxyiodide

The first attempted synthesis of methylammonium oxyiodide followed a previously reported synthesis of bismuth oxyiodide by Li et al. (2011)[32]. This synthesis involved the addition of a base to a solution of bismuth nitrate/methylammonium nitrate in nitric acid. In the case of bismuth nitrate, this leads to the precipitation of a bismuth oxynitrate species,[38] which is used in subsequent steps. However, such an oxynitrate salt of an organic cation is likely not stable, so no precipitate formed when the synthesis was performed with methylammonium nitrate.

The results of a second attempt at the synthesis of methylammonium oxyiodide, using a similar procedure as the one used for trimethylammonium-N-oxide iodide, are presented below.

Figure 8 shows the powder x-ray diffraction patterns of the product (denoted 'Methylammonium oxyiodide') and the starting material.

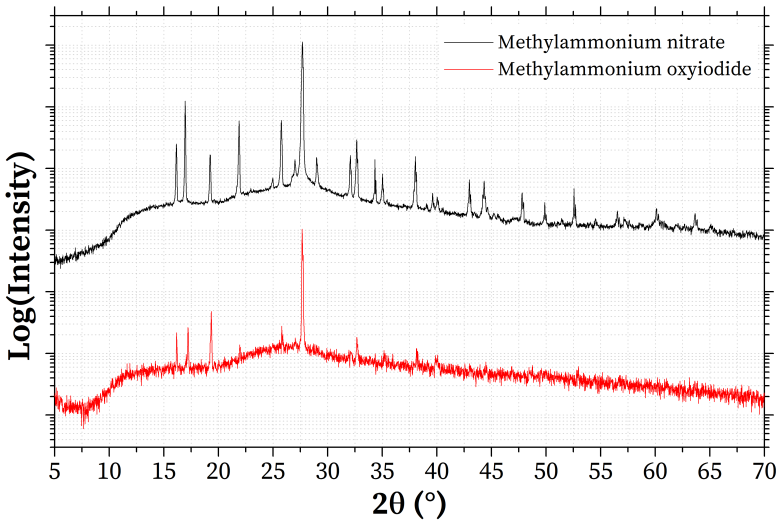

Figure 8: Comparison of the powder XRD patterns of methylammonium nitrate and the methylammonium oxyiodide product. The low intensities of the peaks and the large amorphous background are a result of the presence of some liquid in the sample, either due to the attraction of moisture from the air or partial melting of the sample.

Comparison of these two patterns shows that all of the peaks in the product pattern originate from the methylammonium nitrate starting material. No other product peaks appear to be present. A DSC-TGA measurement was done to confirm that the product consisted of methylammonium nitrate. The result is shown in figure 9. Figure 9a shows the DSC-TGA curves of the product, figure 9b those of the methylammonium nitrate reagent.

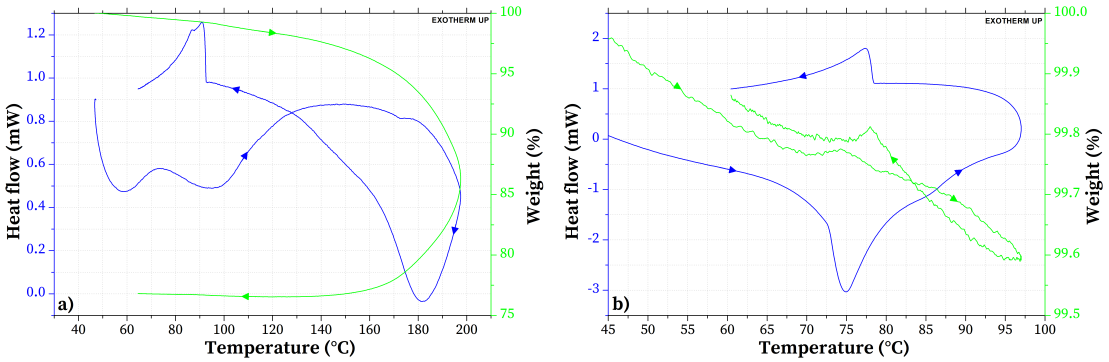

Figure 9: DSC-TGA curves of (a) the methylammonium oxyiodide product drop cast at 140 °C and (b) the methylammonium nitrate reagent.

The DSC curve for methylammonium nitrate shows an endothermic peak at approximately 75 °C, which is close to a solid-to-solid phase transition known to occur in methylammonium nitrate.[39] Little to no weight loss is observed during this measurement. The DSC curve of methylammonium oxyiodide drop cast at 140 °C shows broad peaks at low temperature, which are likely due to evaporation of ethanol used during synthesis and water attracted from the air. Decomposition is observed at high temperature (above 180 °C), which is consistent with the degradation behavior of methylammonium nitrate.[40] The solid-to-solid phase transition peak is not seen during heating, possibly due to the presence of water which dissolves the methylammonium nitrate. However, the corresponding peak is visible during cooling. Interestingly, the expected melting peak[39] at approximately 110 °C is also not observed.

Both the PXRD and the DSC-TGA results indicate that the product principally contains the methylammonium nitrate starting material. Hence, this synthetic method cannot be used to obtain the desired inverse hybrid perovskite compound.

3.4 Alkali metal antiperovskites

After direct synthesis of an inverse hybrid perovskite proved infeasible, focus shifted to the synthesis of antiperovskites of alkali metal cations with a chalcogen and a halide anion. Such structures had been previously synthesized[27–29,41] and showed absorption of light in the visible region, making them attractive for photovoltaic applications. However, these previous reports focused primarily on the structure of these compounds and did not include measurements of photovoltaic properties.

The choice of alkali metal antiperovskite to study was based on its calculated tolerance factor, see table 4. As with the inverse hybrid perovskites described before, the antiperovskite phase

Table 4: Tolerance factors of a selection of alkali metal/chalcogenide/halide antiperovskites. The underlined values are those that are expected to crystallize in the perovskite phase.

$\mathbf{X_3BA}$	$\mathbf{t_X = Cl}$	$\mathbf{t_X = Br}$	$\mathbf{t_X = I}$
Na_3OX	<u>0.83</u>	<u>0.87</u>	<u>0.94</u>
Na_3SX	0.70	0.74	<u>0.80</u>
Na_3SeX	0.67	0.70	0.76
K_3SX	0.70	0.73	0.79
Rb_3SX	0.70	0.73	0.78
Cs_3SX	0.70	0.73	0.78

favors small B-site anions and large A-site anions. The size of the X-site cation has little to no effect on the tolerance factor. Based on these tolerance factors and the availability of chemicals, sodium oxyiodide and sodium sulfoiodide were selected.

Aside from the expected absorption behavior of the alkali metal antiperovskites themselves, these compounds may also provide a synthetic pathway to inverse hybrid perovskites. Dietzel and Jansen (2001)[42] reported on the ion exchange of cesium by tetramethylammonium in cesium auride. It may be possible to perform a similar ion exchange in an alkali metal antiperovskite. Larger alkali metal cations, such as cesium or rubidium, would be preferred for this purpose as these have ionic radii that are closest to those of organic cations.

3.5 Sodium sulfoiodide

Figure 10 shows precession images of single-crystal XRD data of a crystal obtained from melt crystallization of the sodium sulfoiodide product.

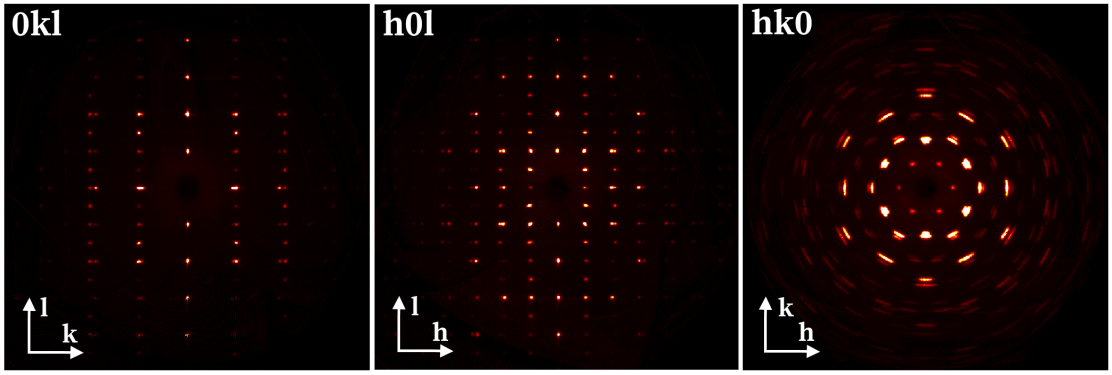

Figure 10: Precession images of a crystal of the sodium sulfoiodide product obtained from melt crystallization. The systematic absences present in these images indicate a primitive hexagonal or base-centered orthorhombic structure with a 2_1, 4_2 or 6_3 screw axis along the **c** axis of the unit cell. However, accurate space group determination and structure solution could not be performed due to the spreading of the diffraction spots. Two domains appear to be present in the crystal, as evidenced by the double spots along the **a** and **b** axes.

The images show spots which are somewhat smeared out in circles perpendicular to the [001] direction, indicating that there may be some rotational disorder around this axis. Additionally, there are extra spots in the [100] and [010] directions. Hence, more than one domain may be present in the sample. Due to the smeared out spots, structure solution from this data proved difficult. Energy-dispersive spectroscopy (EDS) was performed on the material to determine which elements are present, the results of which are displayed in figure 11.

The spectrum shows the presence of carbon (likely from the sample holder), oxygen, sodium and sulfur. The ratio of atomic percentages of these elements in the sample is 2:2:1 respectively. Interestingly, iodine is almost completely absent, possibly due to evaporation of sodium iodide during synthesis. Considering these elements and the amounts in which they are present in the sample, sodium sulfate seems to have formed instead of the desired sodium sulfoiodide. The amount of oxygen in the sample is lower than would be expected for sodium sulfate, but this can be explained by the lower sensitivity of EDS to elements with low atomic numbers.

Several phases of sodium sulfate are known to exist.[43] Of these, the cell parameters[44] of sodium sulfate III are close to those calculated from the single-crystal XRD data and the systematic absences expected for its space group—*Pbnn*—are also observed here, with one exception. The reflection condition *h0l: h + l = 2n* expected for the *Pbnn* space group is not obeyed in the data presented above. A possible explanation for this fact is the presence of multiple domains in the crystal, which are rotated through 90° around the [001] axis with respect to each other. This finding is in agreement with the previously noted rotational disorder around the same axis. Sodium sulfate III is the stable phase of sodium sulfate between 185 °C and 241 °C. Nevertheless,

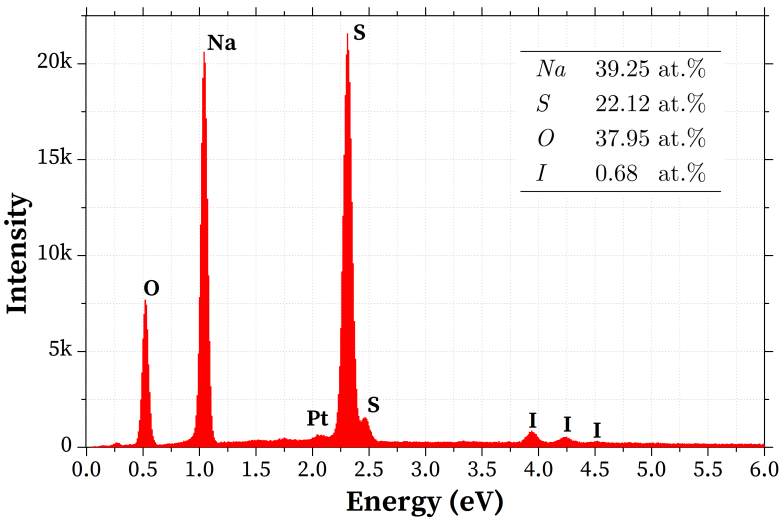

Figure 11: Energy dispersive spectrum of the sodium sulfoiodide product obtained by melt crystallization. The spectrum shows the absence of a significant amount of iodine in the sample. The inset contains the elemental composition calculated from this spectrum.

this phase of sodium sulfate is known to exist in a metastable state even at room temperature.[43]

Several experiments were performed to confirm that sodium sulfate was indeed formed. Firstly, some of the crystalline product was added to ethanol and left for several days. Both of the reagents of the synthesis are known to dissolve in ethanol and the desired product is also expected to dissolve. Conversely, sodium sulfate is completely insoluble. After several days, it was indeed found that the product had not dissolved appreciably in the solvent. The remaining product crystals were then ground in a mortar and used for powder x-ray diffraction. The results are shown in figure 12.

A good Rietveld fit is obtained by using a combination of a sodium sulfate III phase and a sodium sulfate IV phase. A single impurity peak is observed at $2\theta \approx 40°$; the identity of this impurity is unknown. The phase fraction of sodium sulfate III in this sample is approximately 50 %, though a larger fraction was observed in the same sample in an earlier measurement. Hence, sodium sulfate III likely transformed to the stable sodium sulfate IV phase over time or under the influence of atmospheric moisture or oxygen. Interestingly, the hydrated form of sodium sulfate is not observed at all in this sample, despite it having spent several hours in atmospheric conditions and sodium sulfate being known to attract water from the air. Final confirmation of the identity of the product was obtained from differential scanning calorimetry, see figure 13.The small endothermic peaks in the DSC trace at approximately 185 °C corresponds to the transition of a small amount of sodium sulfate IV in the sample to sodium sulfate III. The subsequent peak at approximately 240 °C results from the transformation of sodium sulfate III to sodium sulfate I.[43] A large endothermic melting peak of sodium sulfate is observed at approximately 880 °C, close to the expected melting point. A corresponding exothermic peak is observed upon cooling. Some decomposition of sodium sulfate also occurs close to and above the melting point.

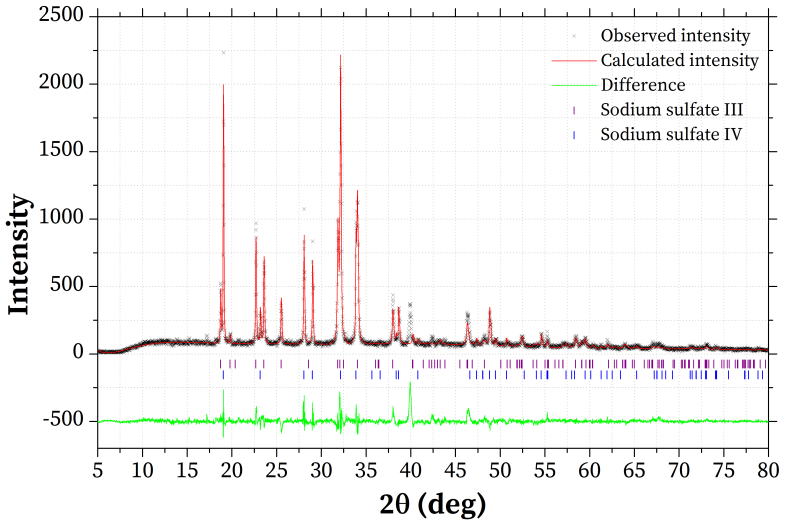

Figure 12: Powder XRD pattern of the sodium sulfoiodide product with a Rietveld fit. The pattern is fitted well using two sodium sulfate phases. An impurity peak is observed at approximately 40° 2θ. The source of this peak is unknown.

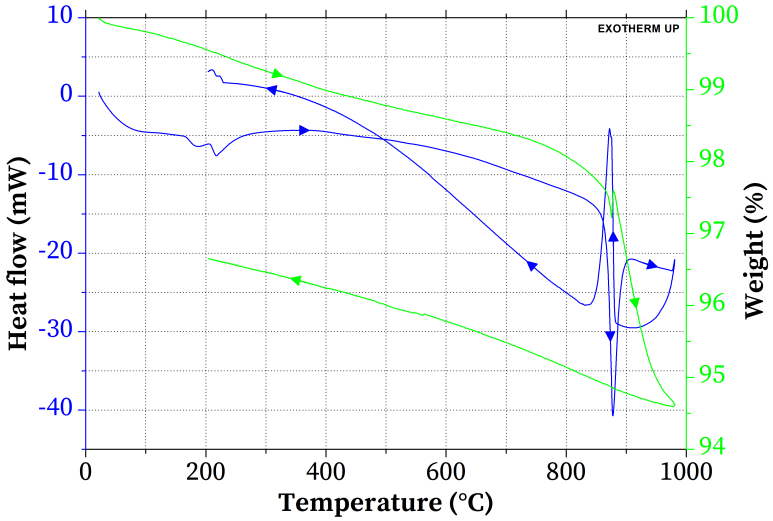

Figure 13: DSC-TGA trace of a crystal of the sodium sulfoiodide product. The two peaks at approximately 200 °C are due to transitions from sodium sulfate IV to sodium sulfate III, which is expected at 185 °C, and from sodium sulfate III to sodium sulfate I.[43] The large peak at 880 °C is the result of melting of sodium sulfate.

Each of the results described above confirms the formation of sodium sulfate as the product rather than the desired sodium sulfoiodide. The origin of oxygen in this sample is not completely clear as oxygen was excluded from the reaction vessel during the synthesis and the reagents were dried and handled in an inert atmosphere. Nonetheless, it is not inconceivable that some water may have remained in the reagents, which reacted with sodium sulfide or sodium polysulfides present in the reaction mixture.

3.6 Sodium oxyiodide

The solid-state reaction of sodium iodide and sodium oxide in a platinum crucible yielded a white, sintered powder with some purple discoloration where the powder touched the platinum crucible. The product obtained from melt crystallization in a quartz ampoule appeared more crystalline and showed no purple discoloration. Hence, the discoloration is likely due to either a reaction of the reagents or product with platinum or some platinum-catalyzed reaction. The latter is most likely as energy dispersive spectroscopy showed that there was not a significant amount of platinum in this discolored part of the product.

Figure 14 shows powder XRD patterns of the white part of the product of the solid state reaction and the product of the melt crystallization.

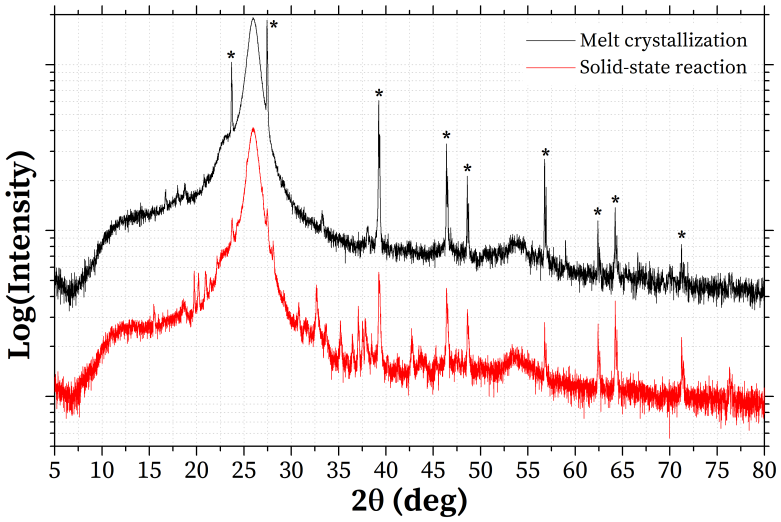

Figure 14: Powder XRD pattern of the sodium oxyiodide product obtained from solid state reaction in a platinum crucible and melt crystallization in a quartz ampoule. The obtained product consisted mostly of unreacted sodium iodide—indicated using a ∗—in both cases. The high-intensity peak at approximately 26° originates from the Mylar film used to cover the sample.

Both patterns show strong peaks for the sodium iodide reagent, as well as some weaker peaks. The identity of these peaks is difficult to determine due to the presence of a Mylar film and degradation of the sample before and during the measurement. The most likely candidates include the hydrate of sodium iodide, sodium peroxide (which was present as part of the starting

materials) and sodium hydroxide, which may have formed by a reaction of sodium (per)oxide with water. This reaction may have occurred either during the synthesis or during the measurement.

DSC-TGA curves of the melt crystallized product are shown in figure 15.

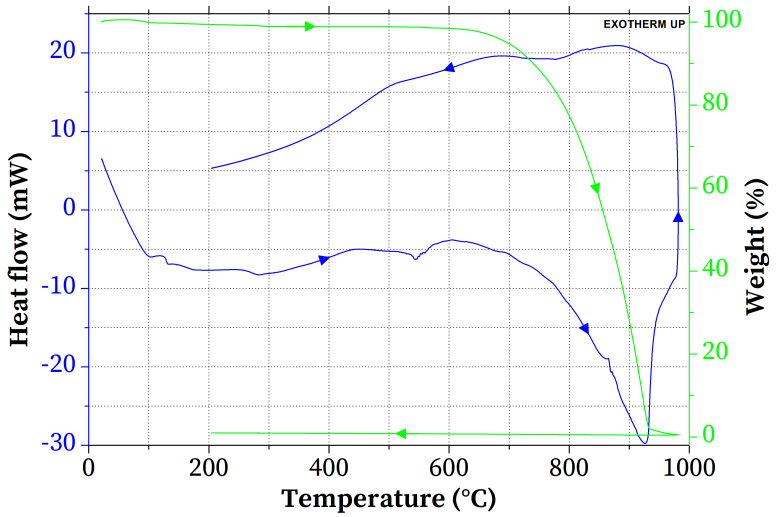

Figure 15: DSC-TGA curves of the sodium oxyiodide product obtained from melt crystallization in a quartz ampoule between room temperature and 1000 °C at a rate of 20 °C/min.

Only a single endothermic peak with a corresponding weight loss was observed at approximately 900 °C. This peak most likely corresponds to the evaporation of sodium iodide and concurrent decomposition of sodium (per)oxide into sodium metal—which evaporates at this temperature—and oxygen.

Table 5 shows the elemental composition of the products from the solid-state reaction and from melt crystallization measured by energy dispersive spectroscopy. Both are close to each other and to the composition of the reagents, though the amount of iodine and oxygen are lower than expected due to the formation of oxygen and evaporation of sodium iodide.

Table 5: EDS results of the sodium oxyiodide product obtained from solid-state reaction and melt crystallization as well as those of the black crystal obtained from flux growth.

Element	**Solid-state reaction (%)**	**Melt crystallization (%)**	**Black crystal (%)**
Na	66.5	64.8	51.2 ± 2.78
I	16.5	16.0	14.2 ± 0.62
O	17.0	19.3	32.4 ± 1.63
Pt	—	—	2.21 ± 1.22

More interesting results were obtained from the attempted flux growth of sodium oxyiodide. Although the desired compound was not formed—the product mixture consisted primarily of sodium iodide flux—some small, black crystals were left behind after dissolution of the flux in glycerin. These crystals were shown to contain platinum by energy dispersive spectroscopy (see

table 5, rightmost column). Single-crystal XRD measurements yielded the precession images displayed in figure 16.

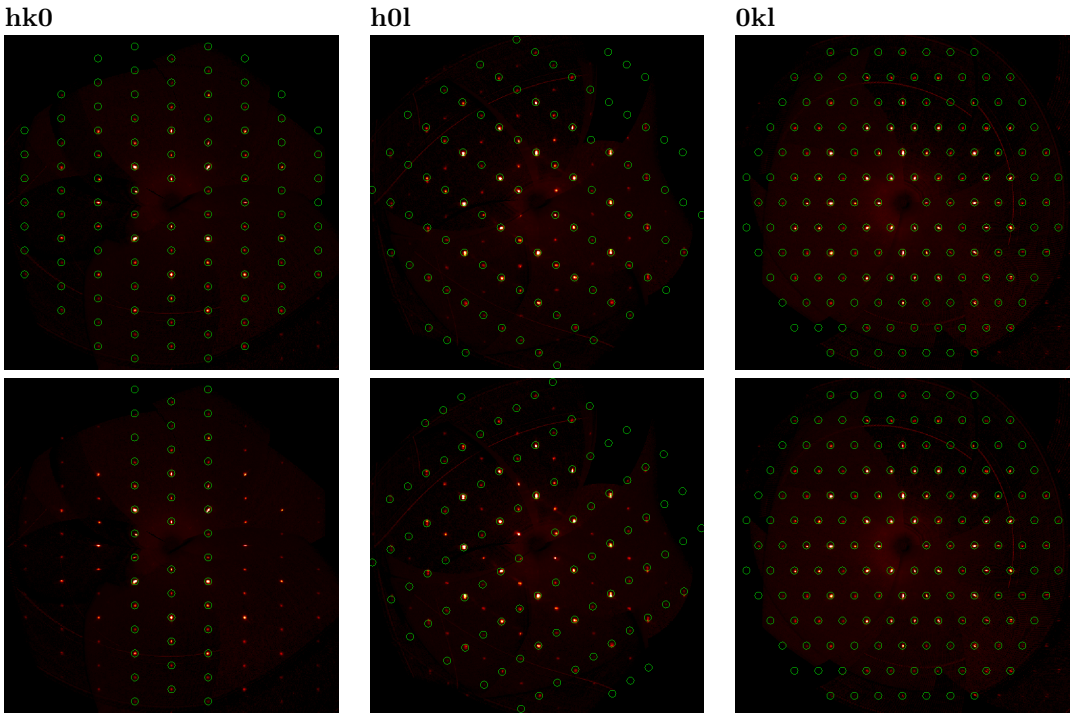

Figure 16: Precession images of a sodium orthoperiodate crystal with two twin domains. Green circles indicate the diffraction spots that belong to the first (top row) and the second (bottom row) domain.

The diffraction pattern can be well explained by a coexistence of two twin domains of a monoclinic structure with the cell parameters in table 6. The two domains are related to each other by a 180° rotation around the [101] axis of the (direct space) unit cell. The diffraction spots belonging to each of the twin domains are indicated in figure 16 using green circles.

The structure of the product was solved and refined from the single-crystal XRD data, yielding the structure displayed in figure 17. The structure contains isolated octahedral IO_6 groups with sodium cations between them. These results correspond well to the previously reported[45] unit cell parameters of sodium orthoperiodate (Na_5IO_6). In this report, the unit cell of sodium orthoperiodate was found from powder XRD data by comparing to the structures of Na_5ReO_6 and Li_5ReO_6 as single-crystals of this sodium orthoperiodate could not be grown. It is indeed found that the sodium orthoperiodate is isostructural to these perrhenate materials. To my knowledge, the growth of single crystals of (anhydrous) sodium periodate has not been reported in the literature. The elemental composition of the product was measured by energy dispersive spectroscopy. The results are listed in table 5. The ratio of sodium to iodine is close to the expected value for sodium orthoperiodate, but the amount of oxygen is lower than expected. This may again be due to the lower sensitivity of the EDS detector to elements with a low atomic

Table 6: Cell parameters of the sodium orthoperiodate structure.

Space group	C2/m
a	5.6987(5) Å
b	9.7734(7) Å
c	5.6318(5) Å
α	90°
β	111.383(4)°
γ	90°
V	292.08(4) Å^3

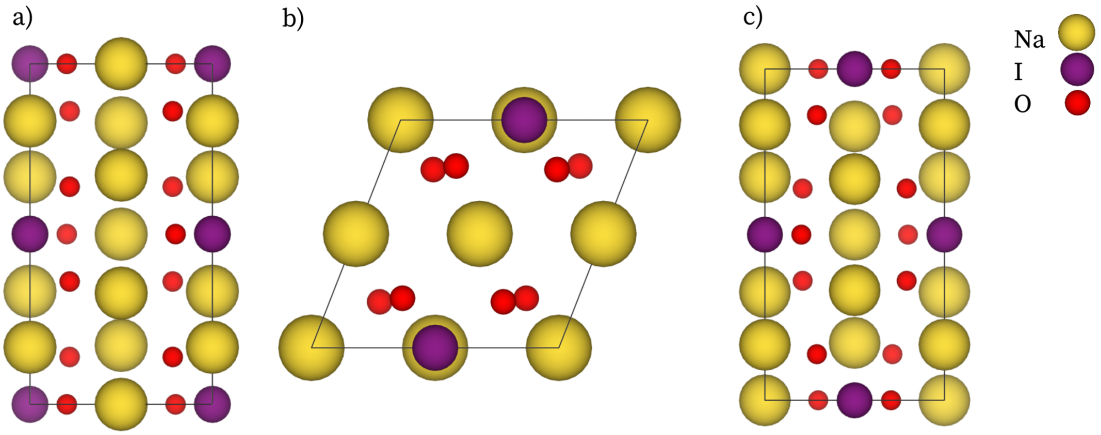

Figure 17: Structure of sodium orthoperiodate along the **a**, **b** and **c** directions solved from the single-crystal XRD data.

number.

Figure 18 shows DSC-TGA curves of the sodium orthoperiodate product. The TGA curve shows four weight loss steps, at 150 °C, 250 °C, 480 °C and 840 °C, each of which is accompanied by an endothermic peak in the DSC curve. The first may be the result of the decomposition of a hydrate of sodium orthoperiodate and the final weight loss probably corresponds to the decomposition of sodium orthoperiodate itself. The nature of the other two weight loss steps is unknown. More detailed study of the decomposition behavior of this compound will be required.

The presence of sodium orthoperiodate is somewhat surprising as periodates are usually synthesized from iodates electrochemically or using chloride gas in aqueous conditions:[46]

$$IO_3^- + 6\,OH^- \longrightarrow IO_6^{5-} + 3\,H_2O + 2\,e^- \qquad \textit{Electrochemical}$$

$$IO_3^- + 6\,OH^- + Cl_2 \longrightarrow IO_6^{5-} + 3\,H_2O + 2\,Cl^- \qquad \textit{Reaction with chlorine}$$

An alternative reaction was reported[45] in which sodium metaperiodate was reacted with sodium oxide. However, in each of these reactions, an iodate—in which iodine has an oxidation state of +5, only 2 lower than the +7 oxidation state of iodine in periodates—or another periodate is used as the source of iodine. However, the only source of iodine available to the reaction here is sodium iodide, in which iodine has an oxidation state of -1. Hence, a very large change in the oxidation number of iodine must be achieved for this reaction to occur. At this time, the

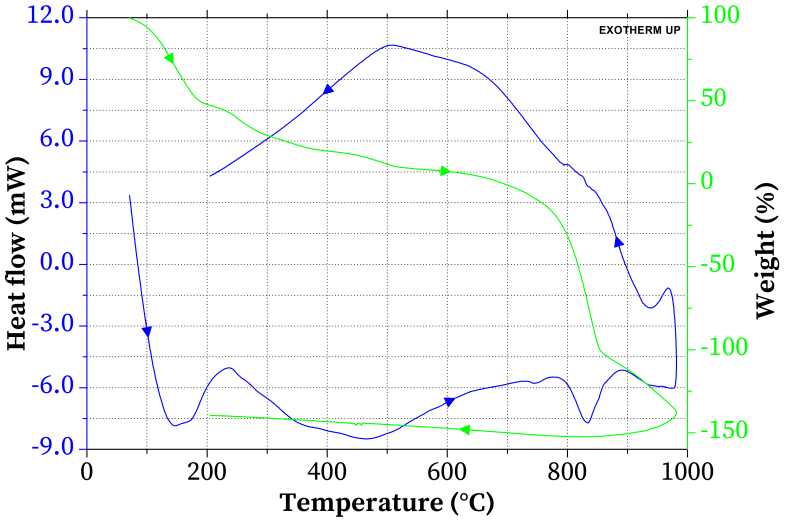

Figure 18: DSC-TGA curves of the sodium orthoperiodate crystals. Four weight losses are observed, at 150 °C, 250 °C, 480 °C and 840 °C. Each of these is accompanied by an endothermic peak in the DSC curve. The final weight of the sample is below 0 % due to a measurement error, but the qualitative behavior of the sample can nevertheless be assessed.

mechanism of this reaction is still poorly understood and requires further investigation. It does not appear that a direct synthesis of (per)iodates from an iodide is known.[46]

Periodates find application as strong oxidizers in inorganic and organic chemistry, for example for the cleavage of 1,2-diols and α-diketones. Additionally, they can be used in the stabilization of high oxidation state transition metal complexes and even as part of pyrotechnics formulations.[46,47]

4 Conclusion

The goal of this project was the synthesis and characterization of hybrid (IHP) and alkali metal-based inorganic inverse perovskites. Specifically, it involved the synthesis of trimethylammonium oxyiodide, methylammonium oxyiodide (both inverse hybrid perovskites), sodium sulfoiodide and sodium oxyiodide (inorganic inverse perovskites). Unfortunately, none of the desired inverse perovskite products was actually formed. Nonetheless, some interesting results were obtained.

A critical view of the literature shows that only a small number of the theoretically predicted IHPs is likely to be experimentally accessible and expected to crystallize in the inverse perovskite phase. A similar conclusion can be drawn for inorganic antiperovskites. In both cases, small B-site ions are required for the antiperovskite phase.

The synthesis of the trimethylammonium IHP did not succeed due to the presence of a covalent nitrogen-oxygen bond in the trimethylamine-N-oxide reagent. A similar ionic species is unstable due to the high basicity of the oxide anion. Reaction of the covalent trimethylamine-N-oxide with hydroiodic acid instead yielded trimethylammonium-N-oxide iodide, the identity of which was confirmed by single-crystal XRD, DSC-TGA and elemental (CHN) analysis. The crystal structure of the product—which, to my knowledge, has not been reported in the literature—was determined by single-crystal XRD and consists of alternating layers of hydrogen-bonded trimethylamine-N-oxide molecules and iodide anions.

The attempted synthesis of methylammonium oxyiodide did not yield any product, but only recovers the methylammonium nitrate reagent, as shown by powder XRD and DSC-TGA.

Synthesis of sodium sulfoiodide by solid-state reaction and melt crystallization led to the formation of sodium sulfate rather than the desired antiperovskite, possibly due to the presence of some water in the reaction mixture.

Finally, the synthesis of sodium oxyiodide by a solid-state method or melt crystallization primarily yielded the starting reagents without the antiperovskite product. However, sodium orthoperiodate crystals formed during flux growth of sodium oxyiodide through a yet unknown reaction. The first direct determination of the structure of this compound was reported.

4.1 Recommendations for further research

Several potential opportunities for further research can be distinguished. Firstly, trimethylammonium oxyiodide is expected to be unstable due to the high basicity of the oxide anion. Substituting a larger, less basic chalcogen—such as sulfur, selenium or tellurium—for this anion may make the product more stable and easier to attain experimentally. These compounds would not be expected to crystallize in the inverse perovskite structure due to their lower tolerance factor, but they may nonetheless exhibit interesting properties.

Secondly, inverse perovskites allow for monovalent anions on the B-site, contrary to ordinary perovskites. Hence, a compound with a small monovalent anion, such as (tri)methylammonium fluoride telluride (MA_3FTe), may form a stable inverse perovskite with the monovalent ion on the B-site.

Third, the few reports of inverse hybrid perovskites that have been published to date have

used polyatomic anions on the A-site and B-site. Many more polyatomic anions are available and could be used to form inverse perovskites. These could even include transition metals (for example as part of a carbonyl complex) which could impart advantageous optical properties to the perovskite.

Fourth, the effect of increased hydrogen bonding with the organic cation should be investigated as it may improve the stability of the perovskite phase.

With regards to the inorganic antiperovskites, there are also several open questions. The synthesis of the alkali metal antiperovskites should be repeated with better quality reagents and possibly different synthetic methods to determine whether the antiperovskite phase can actually be formed.

If synthesis of the antiperovskite phase can indeed be achieved, cation exchange of the alkali metal for an organic cation should be investigated as an alternative pathway to inverse hybrid perovskites.

Finally, the synthesis of sodium orthoperiodate should be repeated and its reaction mechanism investigated. Subsequently, its properties could be studied.

References

(1) Snaith, H. J. Perovskites: The emergence of a new era for low-cost, high-efficiency solar cells. *Journal of Physical Chemistry Letters* **2013**, *4*, 3623–3630.

(2) Green, M. A.; Ho-Baillie, A.; Snaith, H. J. The emergence of perovskite solar cells. *Nat. Photonics* **2014**, *8*, 506–514.

(3) Mitzi, D. B. In *Progress in Inorganic Chemistry*; Vol. 48, pp 1–121.

(4) Li, W.; Wang, Z.; Deschler, F.; Gao, S.; Friend, R. H.; Cheetham, A. K. Chemically diverse and multifunctional hybrid organic–inorganic perovskites. *Nature Reviews Materials* **2017**, *2*, 16099.

(5) Gray, J. L., *The Physics of the Solar Cell*, 2011, pp 82–129.

(6) Hersch, P.; Zweibel, K. *Basic Photovoltaic Principles and Methods*; tech. rep.; 1982.

(7) Polman, A.; Knight, M.; Garnett, E. C.; Ehrler, B.; Sinke, W. C. Photovoltaic materials: Present efficiencies and future challenges. *Science (80-.).* **2016**, *352*, aad4424–aad4424.

(8) Hara, K.; Arakawa, H.; Dssc, C. In *Handbook of Photovoltaic Science and Engineering*, 2003.

(9) National Renewable Energy Laboratory Perovskite efficiency chart, 2019.

(10) Kieslich, G.; Sun, S.; Cheetham, A. K. Solid-state principles applied to organic–inorganic perovskites: new tricks for an old dog. *Chem. Sci.* **2014**, *5*, 4712–4715.

(11) Li, Z.; Yang, M.; Park, J.-S.; Wei, S.-H.; Berry, J. J.; Zhu, K. Stabilizing Perovskite Structures by Tuning Tolerance Factor: Formation of Formamidinium and Cesium Lead Iodide Solid-State Alloys. *Chemistry of Materials* **2016**, *28*, 284–292.

(12) Shannon, R. D. Revised effective ionic radii and systematic studies of interatomic distances in halides and chalcogenides. *Acta Crystallographica Section A* **1976**, *32*, 751–767.

(13) Li, C.; Lu, X.; Ding, W.; Feng, L.; Gao, Y.; Guo, Z. Formability of ABX 3 (X = F, Cl, Br, I) halide perovskites. *Acta Crystallographica Section B Structural Science* **2008**, *64*, 702–707.

(14) Kieslich, G.; Sun, S.; Cheetham, A. K. An extended Tolerance Factor approach for organic–inorganic perovskites. *Chemical Science* **2015**, *6*, 3430–3433.

(15) Gebhardt, J.; Rappe, A. M. Design of Metal-Halide Inverse-Hybrid Perovskites. *The Journal of Physical Chemistry C* **2018**, *122*, 13872–13883.

(16) Gebhardt, J.; Rappe, A. M. Adding to the Perovskite Universe: Inverse-Hybrid Perovskites. *ACS Energy Letters* **2017**, *2*, 2681–2685.

(17) Gebhardt, J.; Rappe, A. M. Transition metal inverse-hybrid perovskites. *Journal of Materials Chemistry A* **2018**, *6*, 14560–14565.

(18) Ellis, J. E. Adventures with Substances Containing Metals in Negative Oxidation States. *Inorganic Chemistry* **2006**, *45*, 3167–3186.

(19) Niu, G.; Guo, X.; Wang, L. Review of recent progress in chemical stability of perovskite solar cells. *Journal of Materials Chemistry A* **2015**, *3*, 8970–8980.

(20) Wei, Z.; Liao, W.-Q.; Tang, Y.-Y.; Li, P.-F.; Shi, P.-P.; Cai, H.; Xiong, R.-G. Discovery of an Antiperovskite Ferroelectric in [(CH3)3NH]3(MnBr3)(MnBr4). *Journal of the American Chemical Society* **2018**, *140*, 8110–8113.

(21) Li, P.-f.; Tang, Y.-y.; Liao, W.-q.; Shi, P.-p.; Hua, X.-n.; Zhang, Y.; Wei, Z.; Cai, H.; Xiong, R.-g. Experimental Evidence for a Triboluminescent Antiperovskite Ferroelectric: Tris(trimethylammonium) catena -Tri-μ-chloro-manganate(II) Tetrachloromanganate(II). *Angewandte Chemie* **2018**, *130*, 12115–12118.

(22) Batail, P.; Livage, C.; Parkin, S. S. P.; Coulon, C.; Martin, J. D.; Canadell, E. Antiperovskite Structure with Ternary Tetrathiafulvalenium Salts: Construction, Distortion, and Antiferromagnetic Ordering. *Angewandte Chemie International Edition in English* **1991**, *30*, 1498–1500.

(23) Liu, Y.; Yang, Z.; Liu, S. F. Recent Progress in Single-Crystalline Perovskite Research Including Crystal Preparation, Property Evaluation, and Applications. *Advanced Science* **2018**, *5*, 1700471.

(24) Dang, Y.; Ju, D.; Wang, L.; Tao, X. Recent progress in the synthesis of hybrid halide perovskite single crystals. *CrystEngComm* **2016**, *18*, 4476–4484.

(25) Shi, D. et al. Low trap-state density and long carrier diffusion in organolead trihalide perovskite single crystals. *Science* **2015**, *347*, 519–522.

(26) Mitzi, D. A Layered Solution Crystal Growth Technique and the Crystal Structure of $(C_6H_5C_2H_4NH_3)_2PbCl_4$. *Journal of Solid State Chemistry* **1999**, *145*, 694–704.

(27) Feldmann, C.; Jansen, M. Zur kristallchemischen Ahnlichkeit von Aurid- und Halogenid-Ionen. *Zeitschrift für anorganische und allgemeine Chemie* **1995**, *621*, 1907–1912.

(28) Feldmann, C.; Jansen, M. Darstellung und Kristallstruktur von Cs_3ClO. *Zeitschrift für Naturforschung B* **1995**, *50*, 1415–1416.

(29) Sitta, S.; Hippler, K.; Vogt, P.; Sabrowsky, H. Crystal structure of K_3OI. *Zeitschrift für Kristallographie* **1991**, *196*, 193–196.

(30) Pearson, A. J.; Yamamoto, Y. In *Encyclopedia of Reagents for Organic Synthesis*; 3; John Wiley & Sons, Ltd: Chichester, UK, 2010; Vol. 1.

(31) Kurniadi, W.; Brower, K. R. A Reinvestigation of the Thermal Decomposition of Methylammonium Nitrate. *The Journal of Organic Chemistry* **1994**, *59*, 5502–5505.

(32) Li, Y.; Wang, J.; Yao, H.; Dang, L.; Li, Z. Efficient decomposition of organic compounds and reaction mechanism with BiOI photocatalyst under visible light irradiation. *Journal of Molecular Catalysis A: Chemical* **2011**, *334*, 116–122.

(33) Sheldrick, G. M. Crystal structure refinement with SHELXL. *Acta Crystallographica Section C Structural Chemistry* **2015**, *71*, 3–8.

(34) Petříček, V.; Dušek, M.; Palatinus, L. Crystallographic Computing System JANA2006: General features. *Zeitschrift für Kristallographie - Crystalline Materials* **2014**, *229*, 345–352.

(35) Idema, T. Synthesis of Inverse Hybrid Perovskite Structures, MA thesis, 2019.

(36) Dunstan, W. R.; Goulding, E. LXXVI.—The action of alkyl haloids on hydroxylamine. Formation of substituted hydroxylamines and oxamines. *J. Chem. Soc., Trans.* **1899**, *75*, 792–807.

(37) Khuthier, A.-H.; Al-Kazzaz, A. K. S.; Amin, D. Iodometric determination of aryldialkylamine-N-oxides. *Mikrochimica Acta* **1987**, *92*, 249–252.

(38) Lazarini, F. Thermal dehydration of some basic bismuth nitrates. *Thermochimica Acta* **1981**, *46*, 53–55.

(39) Bodo, E.; Postorino, P.; Mangialardo, S.; Piacente, G.; Ramondo, F.; Bosi, F.; Ballirano, P.; Caminiti, R. Structure of the Molten Salt Methyl Ammonium Nitrate Explored by Experiments and Theory. *The Journal of Physical Chemistry B* **2011**, *115*, 13149–13161.

(40) Miron, Y. Thermal decomposition of monomethylamine nitrate. *Journal of Hazardous Materials* **1980**, *3*, 301–321.

(41) Sitta, S.; Hippler, K.; Vogt, P.; Sabrowsky, H. Kristallstruktur von gelbem K_3OBr. *Zeitschrift für anorganische und allgemeine Chemie* **1991**, *597*, 197–200.

(42) Dietzel, P. D. C.; Jansen, M. Synthesis and crystal structure determination of tetramethylammonium auride. *Chemical Communications* **2001**, 2208–2209.

(43) Kracek, F. C.; Ksanda, C. J. The Polymorphism of Sodium Sulphate. IV. *The Journal of Physical Chemistry* **1930**, *34*, 1741–1744.

(44) Frevel, L. K. The Crystal Structure of Sodium Sulfate III. *The Journal of Chemical Physics* **1940**, *8*, 290–290.

(45) Betz, T.; Hoppe, R. Uber Perrhenate II. Zur Kenntnis von Li_5ReO_6 und Na_5ReO_6 - mit einer Bemerkung uber Na_5IO_6. *Zeitschrift für anorganische und allgemeine Chemie* **1984**, *512*, 19–33.

(46) Greenwood, N. N.; Earnshaw, A. In *Chemistry of the Elements*; Elsevier: 1997, pp 872–875.

(47) Moretti, J. D.; Sabatini, J. J.; Chen, G. Periodate Salts as Pyrotechnic Oxidizers: Development of Barium- and Perchlorate-Free Incendiary Formulations. *Angew. Chemie Int. Ed.* **2012**, *51*, 6981–6983.